ADVANCED ENERGY & SUSTAINABILITY RESEARCH
Open Access
www.advenergysustres.com

Elucidating the Energy Storage Performance of 2D Metallic Vanadium Ditelluride/Carbon Nanotube for Next-Generation Asymmetric Supercapacitors Using Emerging MoSSe/Carbon Nanotube

*Sree Raj Koottumvathukkal Anil, Sithara Radhakrishnan, Namsheer Kuniyil, Jung Sang Cho, Sang Mun Jeong, and Chandra Sekhar Rout**

Recently, vanadium ditelluride (VTe_2) a member of the transition metal ditellurdies family has emerged as a functional material for energy storage applications owing to its exotic intrinsic properties. Similar to most of the nanostructured materials, a hybrid structure of VTe_2 is expected to provide enhanced energy storage capability. Herein, two hybrid structures of VTe_2 are engineered using well-explored nanocarbons such as RGO and carbon nanotube (CNT) to create a compelling supercapacitor electrode material. Both the hybrid structures show improved electrochemical activity, but VTe_2/CNT fared better in the charge storage efficiency. The enhanced active sites, short ionic/electronic pathways provided by the CNT network, and the large electric double-layer contribution have synergized for the inflated capacitance of VTe_2/CNT. Further, a high-performance asymmetric supercapacitor (ASC) of VTe_2/CNT//MoSSe/CNT is constructed in a typical Swagelok cell, and the ASC delivered an energy density output of 36.28 Wh kg^{-1} at a power density of 463.16 W kg^{-1} with a remarkable 80.26% capacitance retention. The results of this work suggest that VTe_2/CNT is a promising contender in the pantheon of functional materials for energy storage applications in the near future.

1. Introduction

The impact of the COVID-19 pandemic on the global economy combined with inflated oil prices and climate change synergistically serves as a catalyst that accelerates the global energy crisis. Most renewable energy systems are geographically bound because of that their capability to provide stable energy output is limited.[1] Electrochemical energy storage devices including batteries and supercapacitors are an effective global solution to the energy crisis and a key aspect in transforming the energy sector as a whole.[1,2] The increased research interest in supercapacitors is imputed by their high power density, persistent cycle life, and fast charge/discharge rates.[3,4] At present, the prominent research direction in supercapacitor technology is about improving its energy density.[5] The arrival of novel nanostructured electrode materials has promised to provide high-energy density for supercapacitors.[6,7] The energy storage mechanism in supercapacitors is mostly derived either from an electric double layer or pseudocapacitance.[8,9] Researchers believe that the Faradaic origin of pseudocapacitance will allow a higher amount of energy storage compared to conventional electric double layer capacitors (EDLCs). Many of the newly surfaced nanostructured electrode materials undergo pseudocapacitive mechanisms during the electrochemical energy storage process.[10,11]

2D transition metal dichalcogenides (TMDs) became a promising batch of electrode materials for supercapacitor application with their desirable physicochemical properties including, layered structure and van der Waals (vdW) interaction for ion intercalation, large surface area and active sites for redox

S. R. Koottumvathukkal Anil, S. Radhakrishnan, N. Kuniyil, C. S. Rout
Centre for Nano and Material Sciences
Jain (Deemed-to-be University)
Jain Global Campus, Ramanagaram, Bangalore 562112, India
E-mail: r.chandrasekhar@jainuniversity.ac.in

The ORCID identification number(s) for the author(s) of this article can be found under https://doi.org/10.1002/aesr.202300265.

DOI: 10.1002/aesr.202300265

J. S. Cho
Department of Engineering Chemistry
Chungbuk National University
Cheongju, Chungbuk 28644, Republic of Korea

S. M. Jeong, C. S. Rout
Department of Chemical Engineering
Chungbuk National University
Cheongju, Chungbuk 28644, Republic of Korea

activities, and high theoretical capacitance.[12–14] It has been reported that vanadium-based dichalcogenides such as VS_2 and VSe_2, and their derivatives showed compelling supercapacitor performance.[15-17] Vanadium-based dichalcogenides are thermodynamically more stable than Mo- and W-based chalcogenides and allow fast ion insertion with their inherent layered structure.[18] In the group of vanadium-based dichalcogenides vanadium ditelluride (VTe_2) is least explored in electrochemical reactions. Te has higher electrical conductivity (1×10^2 S m^{-1}) than that of S and Se, which plays a significant role in faster cation insertion reaction kinetics.[19,20] In recent times, there has been a gradual increase in metal telluride-based electrocatalysts for energy storage and electrocatalysis applications.[21–23] Moreover, the lower electronegativity and larger atomic size of Te compared to S and Se allow higher accommodation of electrolyte ions.[24] The strong interlayer coupling between vanadium and tellurium makes VTe_2 more stable than its sulfur and selenium counterparts.[18] Reports suggest that there is a charge transfer between V (*d*) and Te (*p*) through the Te p_z orbitals which sets up VTe_2 for fast charge transfer reactions.[21] Relatively, all 2D materials including VTe_2 suffer from considerable volume expansion during the charge/discharge mechanism and low utilization of the active sites due to ineffective electronic/ionic conductivity during an electrochemical reaction which limits their usage in practical application.[25–27] In this context, incorporation of conductive nanocarbons into these materials can improve their capacitance, rate capability, and reduce their capacity decay by the nanoscale tuning of morphology and chemical structure and widening the interlayer spacing of 2D materials.[28] With VS_2- and VSe_2-based electrodes, it revealed that the nanocarbon additives including carbon nanotubes and graphene have improved their energy storage capability by tuning the electronic and ionic conductivity at the electrode interfaces with enhanced electrochemical stability.[29,30] It is also established that the addition of nanocarbons into TMDs will improve their specific surface area, which plays a significant role in the enhancement of energy storage performance in these composite/hybrid structures.[26] Recently explored vanadium telluride (V_xTe_y)/MWCNT hybrid electrode prepared via SILAR method showed compelling supercapacitor performance. The synergy of EDL and the ion insertion/extraction contributions from MWCNT and V_xTe_y have triggered the superior performance of the electrode.[31] The composition analysis of this study indicates the absence of VTe_2 formation making room for other researchers to work on to attain that.

In this work, we have designed hybrids of VTe_2 with carbon nanotubes (CNT) and reduced graphene oxide (RGO) using a facile hydrothermal method for supercapacitor electrodes. The addition of nanocarbons into the VTe_2 system has improved its capacitance response to multiple folds. Within the framework of this work, the CNT hybrid showed an edge over the RGO one in terms of charge storage capability. We believe the unique three-dimensional architecture of the VTe_2/CNT hybrid and the combination of pseudocapacitive and EDL contributions have enhanced its energy storage performance. We have constructed an asymmetric supercapacitor (ASC) with VTe_2/CNT as the positive electrode. This device delivered a remarkable energy density and a long cycle life.

2. Results and Discussion

2.1. Morphological and Structural Characterizations

The hybrid structures of VTe_2/CNT and VTe_2/RGO and the VTe_2 control sample were synthesized in single-step hydrothermal reactions. The formation of VTe_2 and its nanocarbon hybrid structures are depicted in **Scheme 1** (details may found in the

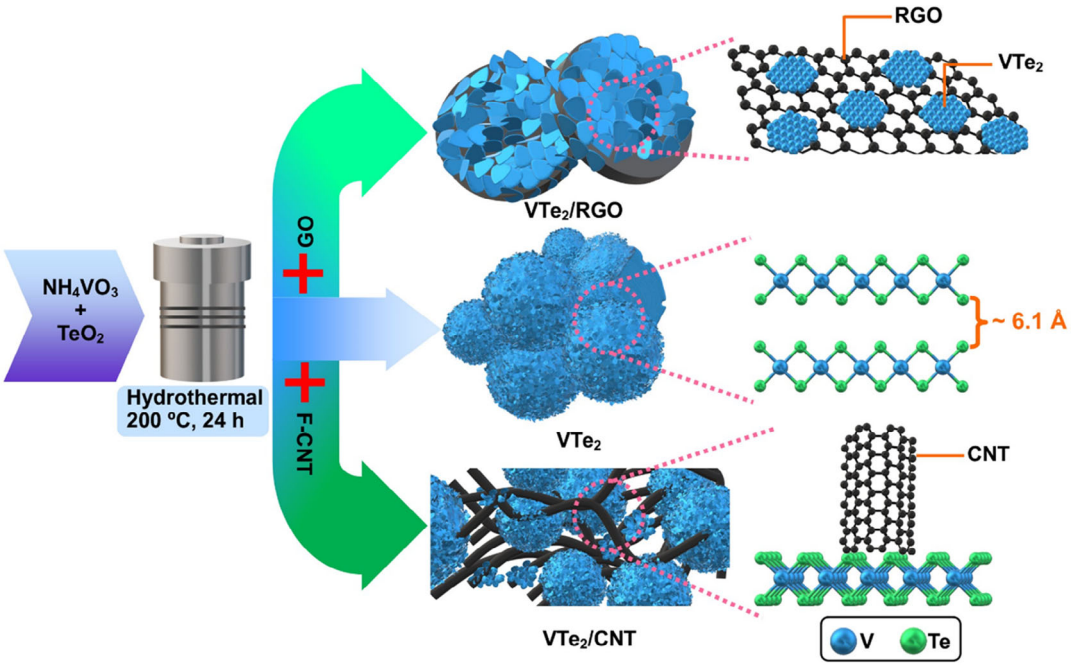

Scheme 1. Illustration of the synthesis routes of VTe_2, VTe_2/RGO, and VTe_2/CNT.

Experimental Section). It is well established that the oxygen functional groups in both CNT (functionalized for this work) and graphene oxide will act as anchoring points for the transition metal ions (V^{4+}) due to electrostatic attraction, which leads to the formation of VTe_2 on them during the hybrid formations.[32,33] Morphologies of all three samples were obtained using a typical FESEM. The FESEM images of VTe_2 reveal a hollow spherical morphology made up of ultrathin nanosheets (**Figure 1**a,b), which is consistent with our previous study.[34] In the case of VTe_2/RGO, the large RGO sheets behave as a growth matrix for the VTe_2 growth (Figure 1c,d). This typical RGO behavior as a novel substrate material allows the vertical growth of VTe_2 arrays on it. The selective growth of VTe_2 on RGO is attributed to the functional groups and the large flat sheet-like morphology of GO. The little free growth of VTe_2 hollow spheres in the solution where RGO sheets were absent supports this observation. However, in VTe_2/CNT a synchronized interconnected 3D structure of VTe_2 hollow spheres and carbon nanotubes can be observed (Figure 1c,d). The highly conductive CNT haystacks support the growth of VTe_2 hollow spheres on it and also interlink other VTe_2 clusters in a similar fashion of an electronic circuit. Even though there are multiple islands of VTe_2 sheets decorated CNT regions, a complete selective growth of VTe_2 nanosheets over CNT similar to RGO is absent here. From the morphological analysis of both the hybrid structures, the self-assembly of VTe_2 on nanocarbons is a positive sign of the interfacial conjugation in them which is a favorable condition for improved supercapacitor performance.[35]

For the crystallographic analysis of prepared samples powder X-ray diffraction (XRD) was employed, and the results are shown in **Figure 2**a. The hydrothermally synthesized VTe_2 hollow spheres exhibited a monoclinic phase in regards to ICSD card 01-077-0309. A drastic change in crystallographic structure in any of the nanocarbon hybrids is absent in the XRD pattern confirming the formation of VTe_2 in both hybrid structures. Moreover, the carbon peaks are absent in the hybrid structures due to the highly crystalline nature of VTe_2 which to an extent suppresses the diffraction signals from both the nanocarbons and the presence of lower concentrations of CNT and RGO in comparison to VTe_2. The Raman spectrum of VTe_2 shows two characteristic peaks located at 114 and 139 cm^{-1} (Figure 2b), which corresponds to the E_g vibration mode of in-plane stretching of V atoms with Te atoms and the out-of-plane A_{1g} vibration mode of Te atoms vibrating in vertical respectively (Figure S1, Supporting Information).[22] The low peak intensity of E_g mode over the A_{1g} band indicates the edge-terminated structure of VTe_2.[36] Interestingly, in the case of both hybrids, we observed a peak broadening and a redshift of the A_{1g} peak. The presence of nanocarbons can reduce the crystallinity of the hybrids which then will be reflected as the weak and broad Raman signals. Along with that, the reduced vdW interaction between VTe_2 and the nanocarbons can also contribute to the broadening and redshift of the A_{1g} peak. In another sense, the short bond length between nanocarbons and VTe_2 and the lattice strain VTe_2 lattice is experiencing due to this can instigate the redshift of A_{1g}. Considering all these observations, they all point to the direction of possible VTe_2/RGO and VTe_2/CNT hybrid formations.[37–39] The presence of nanocarbons in both hybrids is further verified by the Raman spectra in the range of 1200–1800 cm^{-1} (Figure 2c). Two visible Raman signals were detected at 1347 and 1587 cm^{-1} for VTe_2/RGO and 1352 and 1594 cm^{-1} for VTe_2/CNT assigned to the D and G bands of RGO and CNT, respectively.[32] XPS was employed to probe the chemical states and elemental composition in the VTe_2/CNT hybrid system. In the survey spectrum shown in Figure S2a, Supporting Information, the compositional integrity of the

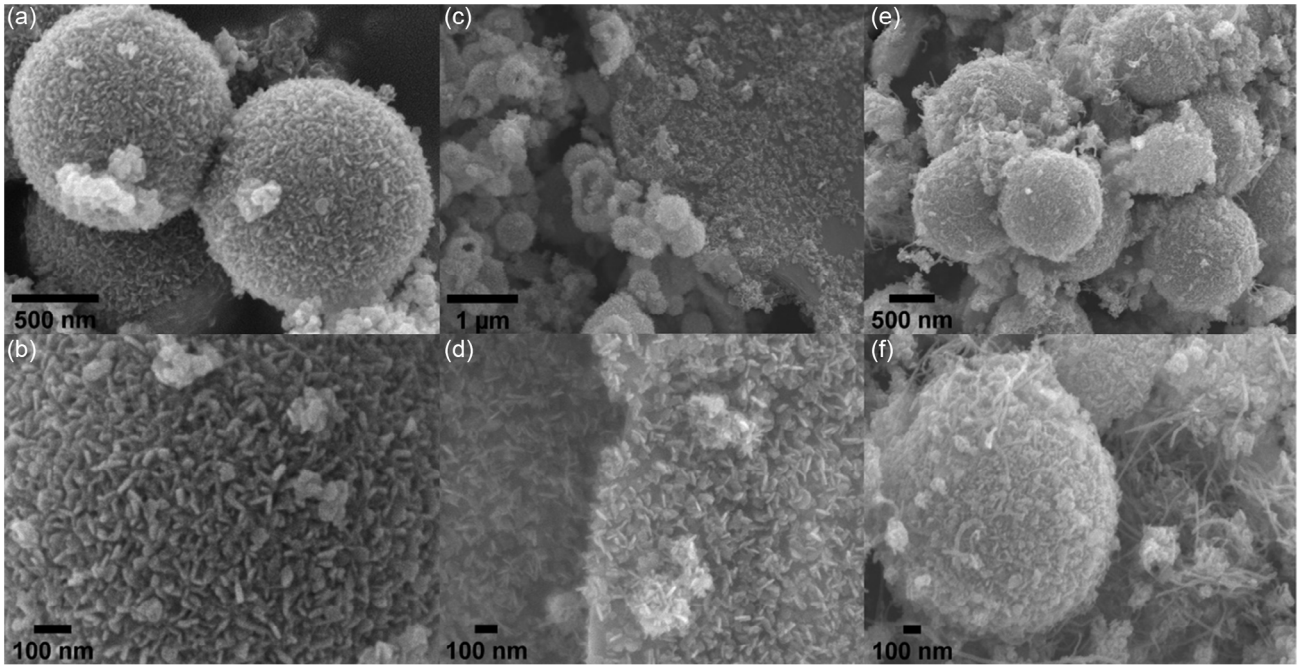

Figure 1. FESEM images of a,b) VTe_2, c,d) VTe_2/RGO, and e,f) VTe_2/CNT.

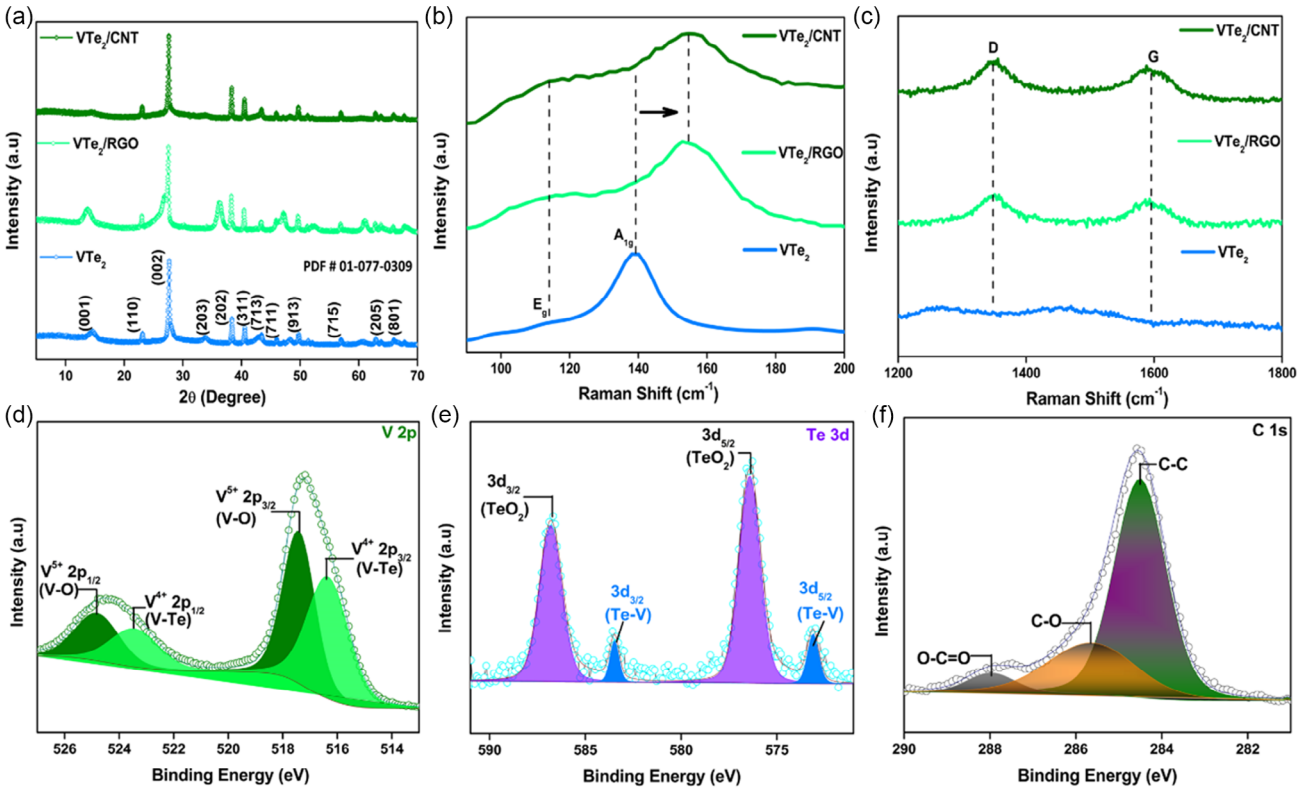

Figure 2. a) XRD pattern of VTe_2, VTe_2/RGO, and VTe_2/CNT, b) magnified Raman signature of the VTe_2 phase, and c) magnified Raman signature of the D and G bands in VTe_2, VTe_2/RGO, and VTe_2/CNT, respectively. High-resolution XPS spectra of component elements d) V 2*p*, e) Te 3*d*, and f) C 1*s* in VTe_2/CNT.

sample is confirmed by the presence of V, Te, and C. The presence of O is unavoidable in a conventional hydrothermal synthesis route. The deconvoluted high-resolution XPS spectra of V 2*p* species exhibited peaks at binding energies 516.3, 517.3, 523.4, and 524.8 eV corresponding to V^{4+} $2p_{3/2}$, V^{5+} $2p_{3/2}$, V^{4+} $2p_{1/2}$, and V^{5+} $2p_{1/2}$ states, respectively (Figure 2d).[21,40] The presence of the +5 state indicates the oxidation of V from +4 during the synthesis. The peak at 530 eV of the deconvoluted O 1*s* spectrum shows the existence of vanadium oxide species (Figure S2b, Supporting Information), which confirms the bonding of +4 species of V with Te. In the deconvoluted Te 3*d* spectrum, two doublet peaks were observed (Figure 2e). The peak observed at 573.1 and 583.4 eV can assigned to the −2 state of Te which then confirms the formation of VTe_2.[22,41] The other pair of peaks located at 576.3 and 586.8 eV corresponds to the TeO_2 species. The detection of TeO_2 in metal ditelluride samples is rather prevalent in literature due to the rapid oxidation of tellurium.[41] Similarly, the core level C 1*s* spectrum corresponds to the CNT is deconvoluted into C—C (284.6 eV), C—O (285.7 eV), and O—C═O (288 eV) bonding in the VTe_2/CNT system (Figure 2f).[32] Even though multiple pathways are possible for the coupling between VTe_2 and CNT while taking into account the fast oxidation of Te species with the atmospheric oxygen, we are inclining to the V—O—C formation pathway in this work. When vanadium ions anchor onto the terminal groups of CNT, the possibility of an oxygen bridge between VTe_2 and CNT emerges owing to the formation of VO_x species and the presence of C—O species. To evaluate the plausibility of this theory, we have investigated O 1s spectra of the sample (Figure S2b, Supporting Information) and observed the presence of V—O—V/Te—O—Te at the binding energy of 530.1 eV, while C═O and C—O observed at 530.8 and 531.5 eV, respectively. When you compare the C 1*s* spectra, the C—O content is higher than C═O but in the O 1*s*, both are in a similar ratio which leads to the possible existence of another oxygen-based species, and V—O—C bonding has the highest probability to satisfy this condition. This oxygen bridge sandwiched by VTe_2 and CNT can act as the origin of the interface of the strong attachment in the VTe_2/CNT hybrid (Figure S2c, Supporting Information).[42,43] Liu et al. also proposed a similar theory of oxygen bridged interfacial coupling in MoS_2/CNT.[42] In concomitant with the notion of similar functional groups also observed in GO, the possibility of forming a similar interface in VTe_2/RGO is also likely.[44] The further investigation and analysis of this interfacial attachment is beyond the scope and focus of this work. The EDX elemental mapping confirms the elemental composition of V, Te, and C and their uniform distribution in the VTe_2/CNT sample (Figure S3, Supporting Information).

2.2. Supercapacitor Performance of VTe_2, VTe_2/RGO, and VTe_2/CNT

To evaluate the electrochemical behavior of VTe_2 and its nanocarbon hybrids, we used a conventional three-electrode setup in

0.5 M K_2SO_4 aqueous electrolyte. Details of the electrode preparation and cell assembly are provided in the experimental section. **Figure 3**a shows the CV loops of VTe_2, VTe_2/RGO, and VTe_2/CNT electrodes at 100 mV s^{-1} in a fixed potential range of −0.4–0.8 V with the same loading mass (1 mg). All three samples exhibited a quasi-rectangular CV shape, a proposed feature of pseudocapacitive behavior.[8] It can be clearly seen that the CV loops of both the nanocarbon hybrids have a larger area compared to pristine VTe_2. This points to the inflated energy storage capability of both the nanocarbon hybrids. In the case of nanocarbon hybrids, VTe_2/CNT has a higher enclosed CV area than VTe_2/RGO, indicating that here VTe_2/CNT has better charge storage capability than its RGO counterpart. Similarly, the GCD curves of all the samples at a specific current of 2 A g^{-1} are displayed in Figure 3b, and the VTe_2/CNT electrode has the longest discharge time, confirming its superior capacitor performance. The GCD curves of all the electrodes are in a skewed triangular shape consistent with the shape of their CV loops. Pristine VTe_2 displays broad redox peaks, which is in line with the intercalation pseudocapacitance mechanism (Figure S4a, Supporting Information). In our previous work, we have established the dominant cationic (K^+) interaction in VTe_2 during the charge storage mechanism.[34] With the addition of nanocarbons, we can see that the behavior of CV loops of the hybrids is slightly shifted into a conventional EDL behavior (Figure 3a) suggesting the presence of a considerable EDL contribution in their charge storage mechanisms. In VTe_2/CNT, this EDL behavior is more prevalent than that of VTe_2/RGO (Figure S4c, Supporting Information). This may be due to the large exposure of CNT regions without VTe_2 growth for electrolyte accessibility. Whereas in VTe_2/RGO, RGO sheets were covered by the VTe_2 growth on them so the direct accessibility to the electrolyte will be less. CV loops of VTe_2/CNT electrode in increased scan rates (10–100 mV s^{-1}) are depicted in Figure 3c. Even at a high scan rate of 100 mV s^{-1}, the VTe_2/CNT electrode maintains its shape, which is a testament to its remarkable reversibility and rate capability. However, at lower scan rates, the CV shape of VTe_2/CNT behaves similarly to that of pristine VTe_2 due to the prolonged impregnation of K^+ ions into the VTe_2 layers with the increased interaction time.[45] This observation is consistent with the possible pseudocapacitive behavior of VTe_2. Figure 3d is the GCD curves of the VTe_2/CNT in an increasing specific current range (1–8 A g^{-1}). The absence of any potential independent region in the GCD curves establishes the EDL and pseudocapacitive behavior of these electrodes. This triangular shape of the GCD curve of VTe_2/CNT reflects the presence of a dominant EDL component in it. The GCD curves of VTe_2 and VTe_2/RGO electrodes are depicted in Figure S4, Supporting Information. Compared to the other two electrodes, VTe_2/CNT exhibited a coulombic efficiency of ≈100% at the low specific current, which is an excellent feature for a good supercapacitor electrode (Figure S5a, Supporting Information). The VTe_2/CNT electrode exhibited a specific capacitance of 255.8 F g^{-1} at 1 A g^{-1} (127.9 mF cm^{-2}, Figure S5b, Supporting Information) with a retention of 74.2% at a higher specific current of 8 A g^{-1}, which is considerably higher than pristine VTe_2 (106.5 F g^{-1}) and VTe_2/RGO (204.5 F g^{-1}) as depicted Figure 3e. EIS was used to study the charge transport and ion diffusion of the prepared samples. Nyquist plots of VTe_2, VTe_2/RGO, and VTe_2/CNT are provided in Figure 3f, and it can be seen that all of them have similar

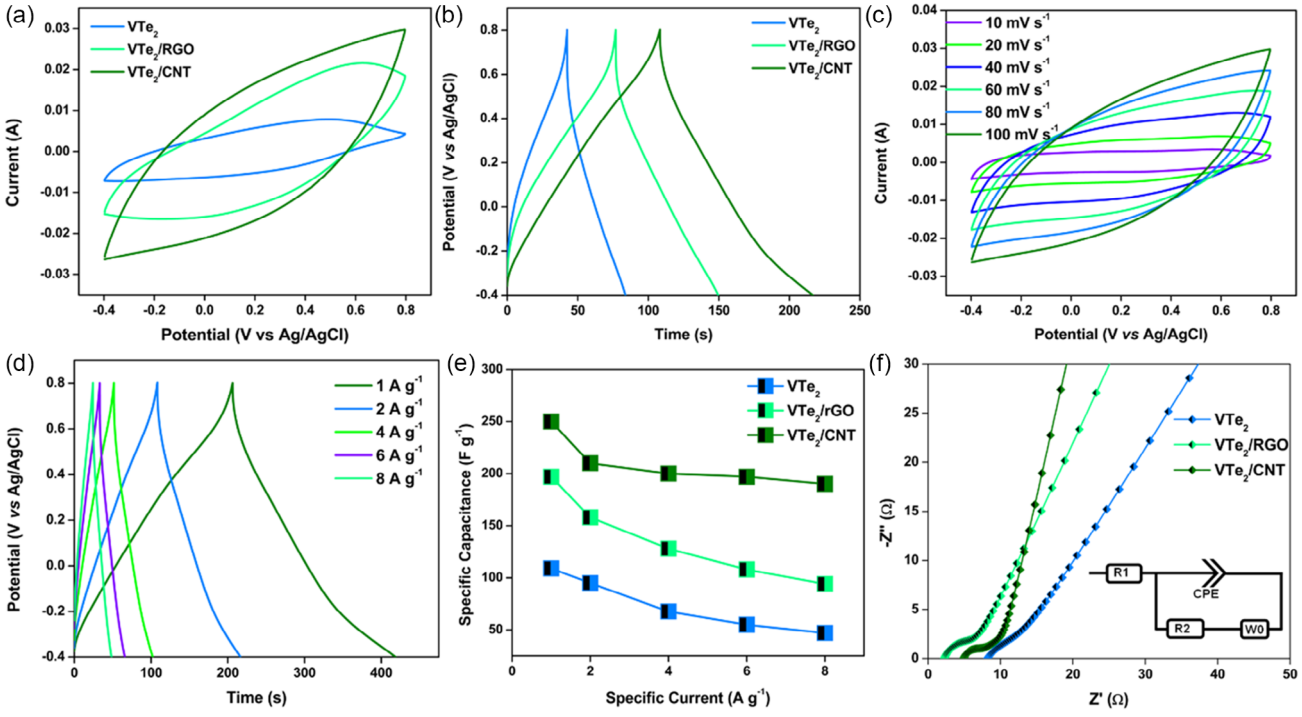

Figure 3. a) Comparative CV loops at 100 mV s^{-1} and b) comparative GCD profile at 2 A g^{-1} of VTe_2, VTe_2/RGO, and VTe_2/CNT electrodes, respectively, in three-electrode configuration, c) CV loops at varying scan rates, and d) GCD profile at varying specific currents of VTe_2/CNT electrode, respectively. e) Specific capacitance vs specific current plot and f) Nyquist plots of all three electrodes.

electrochemical impedance characteristics. The semicircular region of the Nyquist plot at the high-frequency spectrum is assigned to a combined resistance (R_s) and a charge transfer resistance (R_{ct}) (details of these parameters are given in the experimental section). The R_s value of both VTe_2/RGO (2.08 Ω) and VTe_2/CNT (4.78 Ω) is smaller than that of pristine VTe_2 (7.98 Ω). It is evident that the addition of nanocarbons has reduced the intrinsic resistance of the electrode material, which is a common feature in many hybrid systems. Similarly, the R_{ct} values of VTe_2/RGO and VTe_2/CNT are 5.66 and 5.30 Ω, respectively, which is less than that of VTe_2 (8.82 Ω). The reduced R_s value and R_{ct} value contribute to the enhanced charge storage performance in the nanocarbon hybrids by promoting the penetration of the electrolyte. The low R_s value in VTe_2/RGO can be attributed to the improved electrical conductivity due to the hierarchical growth of VTe_2 sheets on highly conductive RGO skeleton. The small interfacial charge transfer impedance in VTe_2/CNT signifies its faster ion diffusion kinetics, which is in tandem with CV and GCD results. The slope gradient of the Warburg impedance observed at the low-frequency region of the Nyquist plot is >45° in all the samples, showing the ion mobility between the electrode surface and the electrolyte. The Warburg impedance reveals a diffusion dormant electrochemical reaction in all three electrodes. In both the nanocarbon hybrids, the Warburg resistance is steeper than the control electrode underscoring the effect of capacitive dominant electrochemical activity.[46] The additional EDL contribution in the electrochemical energy storage due to the exposed CNT of the VTe_2/CNT is hinted by the close to 90° Warburg impedance slope. Bode plots of all three electrodes were used to further evaluate their electrochemical performances (Figure S6a, Supporting Information). It can be seen that the phase angle of the VTe_2/CNT is closer to 90° exhibiting excellent capacitive behavior than other electrodes. To get a better understanding of the frequency responses of these electrodes, we have calculated the relaxation time constant ($\tau_0 = 1/f_0$), where f_0 is the characteristic frequency of the electrode at 45° where the capacitive and resistive impedances will be equal. τ_0 is defined as the minimum time required to discharge all the energy from the capacitor with 50% efficiency.[47] Both the nanocarbon hybrids showed reduced τ_0 values than pristine VTe_2 exhibiting their fast ion diffusion and transport due to the nanocarbon incorporation. The VTe_2/CNT electrode delivered impressive cyclic stability and rate capability after 5000 charge/discharge cycles with a 75% capacitance retention and 100% coulombic efficiency (Figure S6b, Supporting Information).

The integration of nanocarbons into VTe_2 improves the conductivity and shortens the electronic/ionic pathways in the hybrid structure. The presence of nanocarbons multiplies active sites and increases the specific surface area in both systems.[28] Both CNT and RGO provide structural and chemical stability to the hybrid materials by preventing volume expansion and restacking of VTe_2. All these factors simultaneously trigger and promote the electrolyte accessibility in these hybrid structures for the electrolyte ions to intercalate, form an EDL, improve ion diffusion, and enhance the charge transfer during the electrochemical reaction, which eventually emulates the capacitance value to multiple folds. In the RGO hybrid system, the in situ grown VTe_2 nanosheets prevent the restacking of RGO sheets and utilize more active sites to provide better charge storage capability. The large exposed CNT bundles not only amplify the conductivity but also create more electric double-layer capacitance, which mutually contributes to overall electrochemical activity along with the aforementioned activities in the case of VTe_2/CNT.[48] Also, the hollow CNT structure provides better electrochemical stability to give VTe_2/CNT an edge over its RGO counterpart in this study. In the context of this study, we arrive at the conclusion that VTe_2/CNT is the best material but we are open to the possibility that at a different chemical condition, VTe_2/RGO might give better performance because of the excellent plausibility of other TMD/RGO hybrid structures reported before.[26] There is a certain level of unavoidable oxide species present in this material from both V and Te. Electrochemical contributions from these species are a matter for discussion for another aspect of this work which we did not explore here due to various factors.

To give insights into the charge storage mechanism in VTe_2/CNT electrode, the power law was implemented on the CV loops ($i(V) = av^b$, where a and b are the variable coefficients, $i(V)$ is the current a specific potential, and υ is the scan rate). We have distinguished capacitive and diffusive current values by solving k_1 and k_2 parameters using Equation (S5), Supporting Information.[49] The results of this process are illustrated in **Figure 4**a,b (the specific capacitance of the VTe_2/CNT electrode calculated from the CV loops is provided in Figure S5c, Supporting Information). The shaded region in Figure 4a depicts the diffusion-controlled pseudocapacitive portion of the overall capacitance value which is almost 22.3% at 20 mV s^{-1}. From Figure 4b, it is evident that as the scan rate reduced to 10 mV s^{-1}, the electrode/electrolyte interaction time increased and diffusion controlled pseudocapacitive region also increased to 31.6%. In the higher scan rate, the diffusion-controlled capacitance plummets, and the capacitive contribution dominates due to the reduced interaction time between the VTe_2/CNT electrode and the electrolyte at the interface. In Figure 4c, the XRD pattern of the VTe_2/CNT electrode after electrochemical assessment is compared with the same electrode before its testing. The XRD data does not reveal any significant changes to the electrode in terms of the formation of new phases or shifts. This confirms the capacitive dominant process assisted by a reversible pseudocapacitance and the absence of any battery-type Faradaic reactions. The morphology of the VTe_2/CNT electrode has not changed after the electrochemical analysis (Figure S7, Supporting Information), this along with the XRD confirms the electrochemical stability of this fabulous electrode material. The plausible pseudocapacitive reactions of VTe_2 with K^+ ions are given as follows[50–52]

$$(VTe_2)_{surface} + K^+ + e^- \leftrightarrow (VTe_2{}^- - K^+)_{surface} \quad (1)$$

$$VTe_2 + K^+ + e^- \leftrightarrow VTe - TeK \quad (2)$$

A schematic representation of the electrochemical anergy storage mechanism of the VTe_2/CNT electrode is provided in Figure 4d.

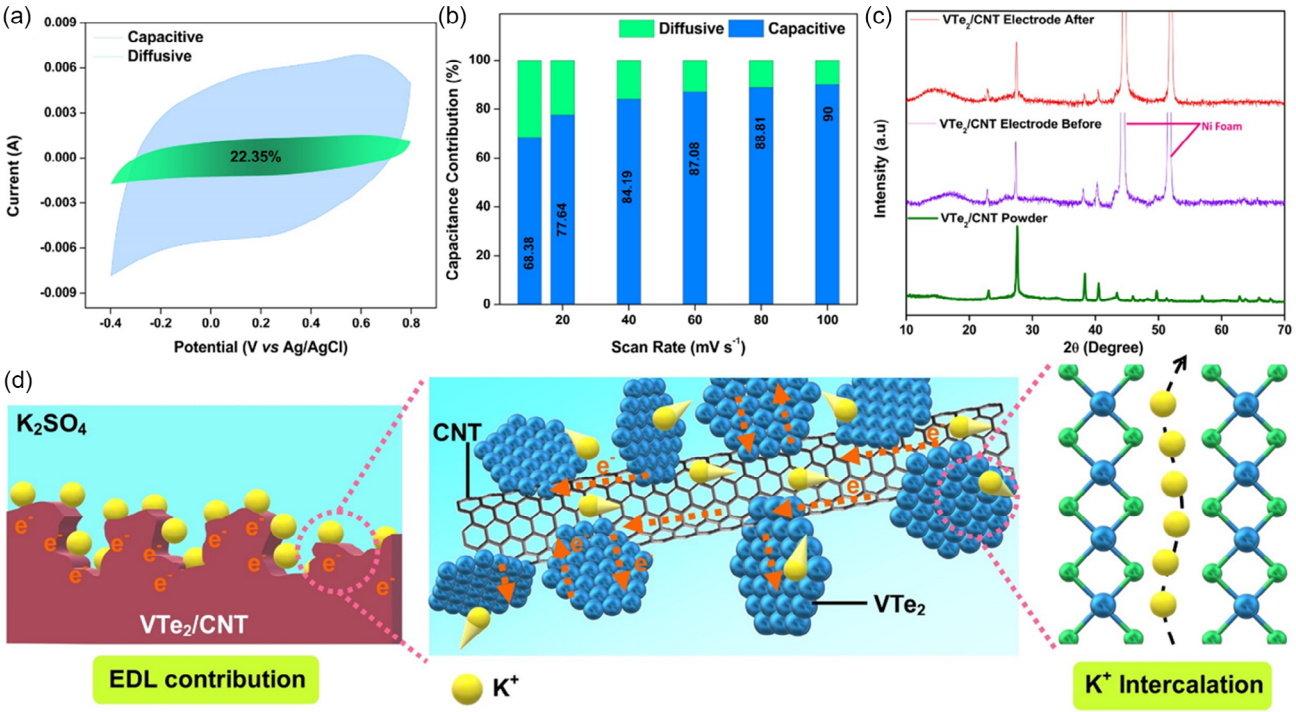

Figure 4. a) Capacitive and diffusion-controlled capacitance in the CV loop of VTe_2/CNT electrode at scan rate of 20 mV s^{-1}, b) capacitive and diffusive contributions in varying scan rates, c) XRD pattern of the VTe_2/CNT electrode before and after the electrochemical analysis, d) schematic illustration of the plausible charge storage mechanism in the VTe_2/CNT electrode.

2.2.1. Performance of the Asymmetric Supercapacitor

To evaluate the energy storage capability of the VTe_2/CNT electrode on a practical scale, an asymmetric supercapacitor was constructed. We have used a conventional Swagelok cell to assemble the ASC with VTe_2/CNT as the positive electrode and MoSSe/CNT as the negative electrode (Figure S11a, Supporting Information, details of the ASC construction can be found in the experimental section). In one of our previous works, we analyzed and established the electrochemical performance of MoSSe/CNT.[53] We are not repeating the detailed material characterization and electrochemical assessment of MoSSe/CNT but for a quick reference, we have provided the XRD pattern and FESEM images of MoSSe/CNT in Figure S8 and S9, Supporting Information, to establish the purity and morphology of the negative electrode. Also, the basic three-electrode analysis of the MoSSe/CNT with the long cyclic study is provided in Figure S10, Supporting Information. **Figure 5**a shows CV loops of VTe_2/CNT and MoSSe/CNT electrodes at a scan rate of 100 mV s^{-1}, which provides the possibility of an ASC with a considerable working window. The charge in both electrodes was balanced using Equation (S6), Supporting Information, the and mass ratio for the device is ≈1:2. The assembled ASC was tested under multiple working windows using CV (Figure 5b) and GCD (Figure S11b, Supporting Information) and noted that beyond 1.6 V the CV loop shows a certain degree of polarization therefore, we consider 0–1.6 V as the stabilized voltage window of this ASC. We have recorded the CV loops and GCD curves of the ASC in incremental scan rates and specific current values, respectively (Figure 5c,d). The analysis of the CV loops and GCD curves of the ASC showed a capacitive behavior with a combination of EDLC and pseudocapacitance similar to both electrodes. The shape of the CV curves does not show any discernable distortion in low scan rates showing the desirable rate capability of the ASC. The specific capacitance calculated from GCD curves exhibits that the ASC has the highest capacitance of 102.04 F g^{-1} at 0.5 A g^{-1} (Figure 5e). The assembled VTe_2/CNT//MoSSe/CNT ASC attained a maximum energy density of 36.28 Wh kg^{-1} at a power density of 463.16 W kg^{-1}, and the ASC performed at a power density of 4434.28 W kg^{-1} with an energy density of 17.24 Wh kg^{-1}. A Ragone plot was used to compare the energy storage performance of this ASC with similar devices (Figure 5f). A detailed compilation of this comparison is provided in Table S1, Supporting Information. We have subjected the ASC under 7000 charge–discharge cycles to measure its electrochemical stability (Figure 5g). Significantly, the ASC showed a capacitance retention of 80.76% with a ≈100% coulombic efficiency after the long cycles. The Nyquist plots of the ASC before and after the cyclic study are reflected in Figure S11c, Supporting Information. The device showed small R_s and R_{ct} values illustrating the excellent electrical contact and low ionic resistance. After the long cycling, the R_s value has not changed signaling no electrode degradation; however, the R_{ct} value is slightly increased due to the interfacial changes of the electrodes in the cell. Similarly, the Warburg slope gradient is also reduced after the stability test, which signifies the reduced momentum of electrolyte ions to the active sites of the electrode. The changes in the Warburg

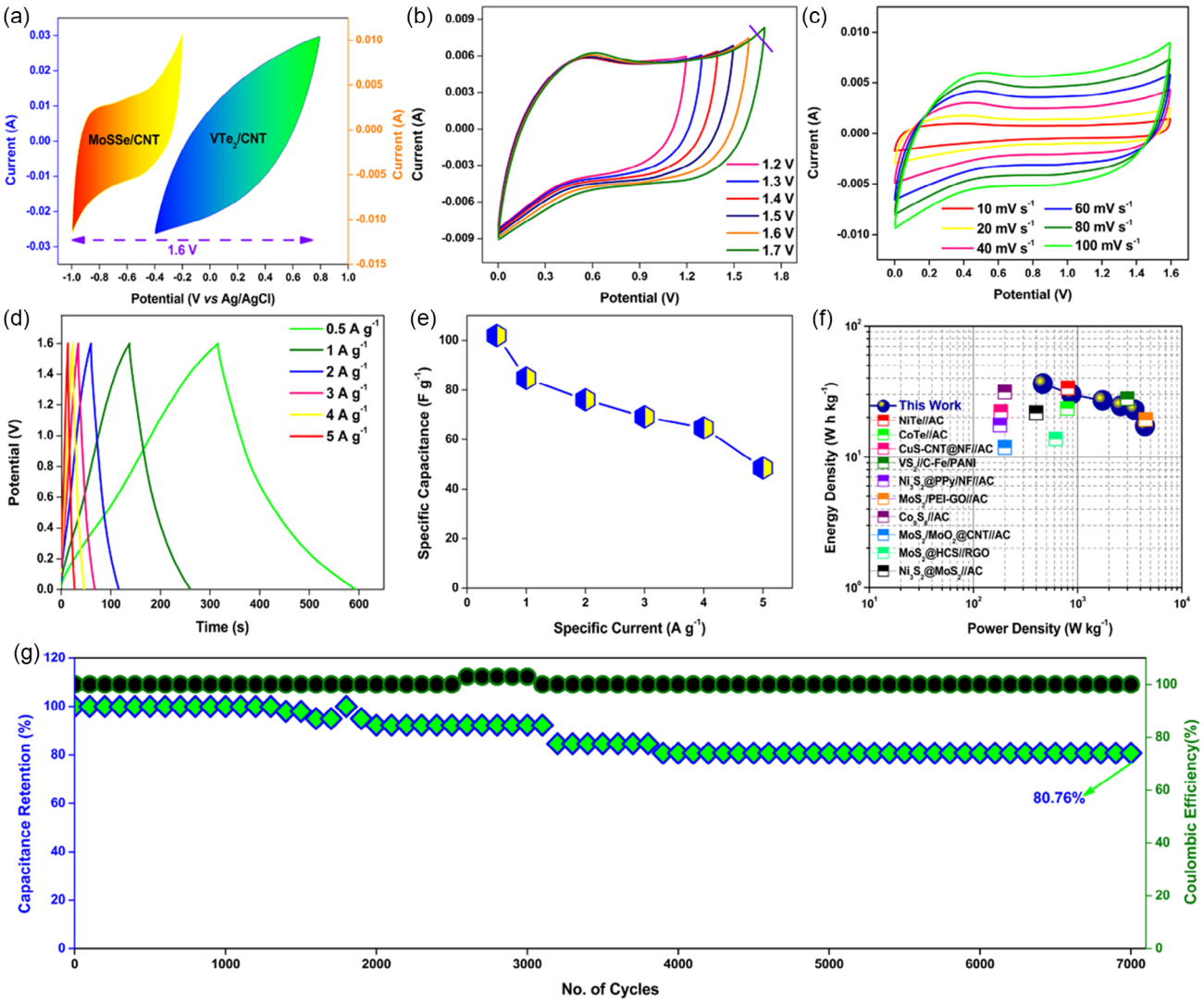

Figure 5. Performance of the ASC. a) CV loops of both positive and negative electrodes at scan rate of 100 mV s^{-1}, b) CV loops of the device in potential windows ranging from 1.2 to 1.7 V at a scan rate of 100 mV s^{-1} and optimized the working window as 1.6 V, c) CV profile of the ASC in varying scan rates, d) GCD profile of the ASC in varying specific current values, e) specific capacitance vs specific current relation of the ASC, f) Ragone plot of the ASC, and g) the capacitance retention of the ASC determined over 7000 cycles at a specific current value of 8 A g^{-1}.

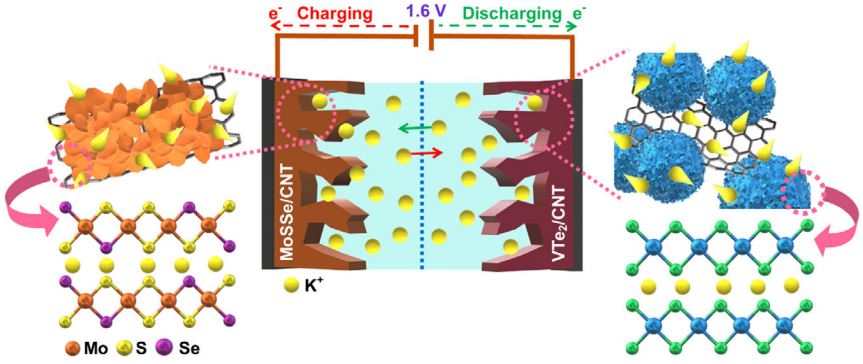

Scheme 2. Illustration of the working of VTe_2/CNT//MoSSe/CNT ASC.

resistance and R_{ct} after 7000 cycles also contribute to the reduced capacitance after cyclic study.[47] The Bode plot suggests the capacitive behavior of the ASC with a phase angle of −68°. After the cyclic test, the capacitive characteristics of the ASC reduce with a phase angle of −53° following a similar trend observed in the Nyquist plot (Figure S11d, Supporting Information). Moreover, we did not observe any considerable reduction in the τ_0 value of the ASC after the cyclic test suggesting the smooth operation of the device even after long charge/discharge cycles. A schematic illustration of the plausible energy storage mechanism in the VTe_2/CNT//MoSSe/CNT ASC is depicted in **Scheme 2**.

3. Conclusions

In this article, we have designed and developed multiple VTe_2 and nanocarbon hybrid structures to evaluate their performance for energy storage using a facile hydrothermal approach. The significant feature of these hybrid structures is the hybridization of pseudocapacitive VTe_2 with highly conducting and well-established EDL materials such as RGO and CNT. Due to the synergistic interaction between VTe_2 and the nanocarbons, the hybrid structures showed improved electrochemical activity in terms of energy storage. When we compared the supercapacitor performance of these hybrid materials, the VTe_2/CNT hybrid outperforms the VTe_2/RGO hybrid. The VTe_2/CNT hybrid structure creates more active sites, and its unique 3D architecture boosts its electrochemical activity. Moreover, we have designed an aqueous electrolyte-based asymmetric supercapacitor with VTe_2/CNT as the positive electrode and MoSSe/CNT as the negative electrode. The constructed ASC delivered an energy density of 36.28 Wh kg^{-1} with an excellent cycle life. The development of rarely explored materials like these and unsealing their true potential by employing various strategies can create high energy density electrode materials, which will revolutionize the appeal of supercapacitors in the energy storage domain.

4. Experimental Section

Chemicals: Ammonium meta vanadate (NH_4VO_3, SDFCL), tellurium dioxide (TeO_2, TCI chemicals), hydrazine hydrate (CDH Fine chemical), ammonium molybdate tetrahydrate ($(NH_4)_6Mo_7O_{24}{\cdot}4H_2O$, SRL chemicals), thiourea (CS (NH_2), SDFCL), selenium metal powder (SDFCL), multiwalled carbon nanotube (<5% impurity, 1–10 µm length, and 3–15 number of walls, Plasma Chem GmbH, Berlin), graphene oxide (GO, Reinste made), H_2SO_4 (SDFCL), HNO_3 (SDFCL), NMP (SDFCL), and DI water.

Materials Synthesis: Synthesis of VTe_2, VTe_2/RGO, and VTe_2/CNT: NH_4VO_3 and TeO_2 were used as the vanadium and tellurium precursors for the synthesis of pristine VTe_2. At first, 85 mg of TeO_2 was treated with 5 mL of hydrazine hydrate. In another container, 585 mg of NH_4VO_3 was dissolved in 40 mL DI water. The hydrazine treated TeO_2 was transferred into the NH_4VO_3 solution and stirred it for some time. This homogeneous mixture was then transferred into a 50 mL Teflon lined stainless steel autoclave for the hydrothermal reaction at 200 °C for 24 h. For the preparation of VTe_2/RGO, 80 mg of GO was added along with the above chemicals. Meanwhile, 80 mg of acid functionalized MWCNT (f- CNT)[30] was added instead of GO for the preparation of VTe_2/CNT. Once the hydrothermal reaction was completed, the residues were washed using DI water and the product was dried in vacuum at 60 °C.

Materials Synthesis: Synthesis of MoSSe/CNT: 1 mmol $(NH_4)_6Mo_7O_{24}{\cdot}4H_2O$ and 7 mmol thiourea were added in 20 mL of ethanol and water mixture (1:1) under vigorous stirring. 5 mL of NMP was then carefully added to this mixture. Then, 3.5 mmol of selenium metal powder treated with 10 mL of hydrazine hydrate was added into the above mixture under constant stirring. Further, 30 mg of f-CNT was added slowly into this reaction mixture and sonicate for 30 min to get a homogeneous dispersion. Then the prepared solution was kept for hydrothermal reaction in a Teflon-lined 50 mL stainless steel autoclave at 200 °C for 24 h.

Materials Characterization: Morphological analysis of the samples was analyzed using a field emission scanning microscope (FESEM, JEOL JSM-7100F, JEOL Ltd., Singapore). The structural characterizations of the samples are carried out using X-ray diffraction (XRD, Rigaku Ultima IV X-ray diffractometer with Ni-filter (Cu Kα, $\lambda = 0.1541$ nm), and Raman spectroscopy is carried out in LABRAM HR (Horiba Jobin Yvon, 488 $\lambda =$ nm). X-ray photo electron spectroscopy (XPS) measurements are performed in a Thermo K-alpha spectrometer using micro focused and monochromated Al Kα radiation with an energy of 1486.6 eV.

Electrochemical Characterization: To assess the electrochemical activity of the electrodes, we have carried out cyclic voltammetry (CV), galvanostatic charge discharge (GCD), and electrochemical impedance spectroscopy (EIS) measurements. All the electrochemical characterizations of all the samples were carried out in a 0.5 M K_2SO_4 electrolyte using a Wuhan Corrtest electrochemical workstation. For the three-electrode configuration, we used a conventional three-electrode cell with Ag/AgCl as the reference electrode and a platinum wire as the counter electrode. The working electrode was prepared by drop casting the mixture of active material (1 mg), Nafion binder (5 µL), and propanol (95 µL) onto a Ni foam substrate. After the drop casting, the Ni foam substrate was then dried and pressed using a typical hydraulic press before incorporating into the cell. EIS measurements are obtained in the frequency range of 0.01 Hz–10 kHz. The Nyquist plot obtained from the EIS has two distinct parts, a semi-circle at high frequency and an oblique line at low frequency. The parameter R_s at the semicircular region represents the combined resistance which involves the intrinsic resistance of the electrode, the ionic resistance of the electrolyte, and the contact resistance between the current collector and the electrode material. During a comparison study such as this, we used similar electrolyte and current collector and electrode loading therefore R_s gives the information on the intrinsic resistance of the electrode material. Where the other parameter R_{ct} measured from the diameter of the semi-circle represents the charge transfer resistance of the electrode. The Warburg impedance at the low frequency region represents the ion-diffusion/transport kinetics of the electrolyte.[25] For the assembly of the asymmetric supercapacitor, we used a Swagelok cell with Whatman filter paper separating the circular electrodes (0.8 cm^2 in area) made up of Ni foam where the electrodes are prepared in a similar fashion as above. The mass balancing between the positive and negative electrodes was achieved using Equation (S6), Supporting Information. The mass ratio of positive and negative electrodes in the asymmetric device is ≈1:2 mg.

Supporting Information

Supporting Information is available from the Wiley Online Library or from the author.

Acknowledgements

The authors gratefully acknowledge financial assistance from the SERB Core Research Grant (grant no. CRG/2022/000897), Department of Science and Technology (grant no. DST/NM/NT/2019/205(G)), and Minor Research Project Grant, Jain University (grant no. JU/MRP/CNMS/29/2023). C.S.R. acknowledges the National Research Foundation of Korea for the Brain Pool program funded by the Ministry of Science and ICT, South Korea (grant no. RS-2023-00222186). This work was supported by the National Research

Foundation of Korea (NRF), and the Commercialization Promotion Agency for R&D Outcomes (COMPA) funded by the Ministry of Science and ICT (grant nos. RS-2023-00217581 and RS-2023-00304768).

Conflict of Interest

The authors declare no conflict of interest.

Data Availability Statement

The data that support the findings of this study are available from the corresponding author upon reasonable request.

Keywords

nanocarbon, pseudocapacitance, supercapacitors, TMDs, VTe_2

Received: November 17, 2023
Revised: January 13, 2024
Published online:

[1] T. Guo, D. Zhou, L. Pang, S. Sun, T. Zhou, J. Su, *Small* **2022**, *18*, 2106360.
[2] F. Xing, Z. Bi, F. Su, F. Liu, Z. S. Wu, *Adv. Energy Mater.* **2022**, *12*, 2200594.
[3] L. Liu, P. L. Taberna, B. Dunn, P. Simon, *ACS Energy Lett.* **2021**, *6*, 4311.
[4] E. Pameté, L. Köps, F. A. Kreth, S. Pohlmann, A. Varzi, T. Brousse, A. Balducci, V. Presser, *Adv. Energy Mater.* **2023**, *13*, 2301008.
[5] H. Zhang, L. Wang, X. Xing, S. Zhao, K. Wang, S. F. Liu, *Adv. Funct. Mater.* **2022**, *32*, 2208403.
[6] S. Liu, S. Sun, X.-Z. You, *Nanoscale* **2014**, *6*, 2037.
[7] J. Jiang, Y. Zhang, P. Nie, G. Xu, M. Shi, J. Wang, Y. Wu, R. Fu, H. Dou, X. Zhang, *Adv. Sustainable Syst.* **2018**, *2*, 1700110.
[8] T. Brousse, D. Bélanger, J. W. Long, *J. Electrochem. Soc.* **2015**, *162*, A5185.
[9] S. Fleischmann, J. B. Mitchell, R. Wang, C. Zhan, D. E. Jiang, V. Presser, V. Augustyn, *Chem. Rev.* **2020**, *120*, 6738.
[10] J. Sun, L. Guo, X. Sun, J. Zhang, L. Hou, L. Li, S. Yang, C. Yuan, *Batteries Supercaps* **2019**, *2*, 820.
[11] P. Nakhanivej, Q. Dou, P. Xiong, H. S. Park, *Acc. Mater. Res.* **2021**, *2*, 86.
[12] B. Chen, D. Chao, E. Liu, M. Jaroniec, N. Zhao, S.-Z. Qiao, *Energy Environ. Sci.* **2020**, *13*, 1096.
[13] D. M. Soares, S. Mukherjee, G. Singh, *Chem. - Eur. J.* **2020**, *26*, 6320.
[14] L. Lin, W. Lei, S. Zhang, Y. Liu, G. G. Wallace, J. Chen, *Energy Storage Mater.* **2019**, *19*, 408.
[15] R. Samal, C. S. Rout, *Adv. Mater. Interfaces* **2020**, *7*, 1901682.
[16] S. Raj KA, P. Mane, S. Radhakrishnan, B. Chakraborty, C. S. Rout, *ACS Appl. Nano Mater.* **2022**, *5*, 4423.
[17] J. Feng, X. Sun, C. Wu, L. Peng, C. Lin, S. Hu, J. Yang, *J. Am. Chem. Soc.* **2011**, *133*, 17832.
[18] J. Shi, Y. Huan, X. Zhao, P. Yang, M. Hong, C. Xie, S. Pennycook, Y. Zhang, *ACS Nano* **2021**, *15*, 1858.
[19] J. He, W. Lv, Y. Chen, K. Wen, C. Xu, W. Zhang, Y. Li, W. Qin, W. He, *ACS Nano* **2017**, *11*, 8144.
[20] J. He, Y. Chen, W. Lv, K. Wen, Z. Wang, W. Zhang, Y. Li, W. Qin, W. He, *ACS Nano* **2016**, *10*, 8837.
[21] U. N. Pan, D. R. Paudel, A. Kumar Das, T. I. Singh, N. H. Kim, J. H. Lee, *Appl. Catal., B* **2022**, *301*, 120780.
[22] T. C. Huang, K. W. Cheng, C. A. Lin, Y. C. Fu, S. K. Lin, Y. Z. Chen, *Sustainable Energy Fuels* **2022**, *6*, 4626.
[23] M. Liu, X. Wang, Z. Huang, P. Guo, Z. Wang, *Mater. Lett.* **2017**, *206*, 229.
[24] G. Zhang, K. Liu, J. Zhou, *J. Mater. Chem. A* **2018**, *6*, 6335.
[25] J. Azadmanjiri, L. Děkanovský, Z. Sofer, *Mater. Today Sustainability* **2023**, *21*, 100322.
[26] J. Cherusseri, N. Choudhary, K. Sambath Kumar, Y. Jung, J. Thomas, *Nanoscale Horiz.* **2019**, *4*, 840.
[27] J. Wang, V. Malgras, Y. Sugahara, Y. Yamauchi, *Nat. Commun.* **2021**, *12*, 3563.
[28] A. Borenstein, O. Hanna, R. Attias, S. Luski, T. Brousse, D. Aurbach, *J. Mater. Chem. A* **2017**, *5*, 12653.
[29] M. F. Koudahi, E. Frąckowiak, *Energy Storage Mater.* **2022**, *49*, 255.
[30] S. Raj KA, A. S. Shajahan, B. Chakraborty, C. S. Rout, *Chem. - Eur. J.* **2020**, *26*, 6662.
[31] B. Pandit, S. R. Rondiya, R. W. Cross, N. Y. Dzade, B. R. Sankapal, *Chem. Eng. J.* **2022**, *429*, 132505.
[32] K. K. Halankar, B. P. Mandal, M. K. Jangid, A. Mukhopadhyay, N. Abharana, C. Nayak, K. Dasgupta, A. K. Tyagi, *J. Alloys Compd.* **2020**, *844*, 156076.
[33] Y. Li, H. Wang, L. Xie, Y. Liang, G. Hong, H. Dai, *J. Am. Chem. Soc.* **2011**, *133*, 7296.
[34] K. A. Sree Raj, N. Barman, S. Radhakrishnan, R. Thapa, C. S. Rout, *J. Mater. Chem. A* **2022**, *10*, 23590.
[35] G. Z. Chen, *Prog. Nat. Sci.: Mater. Int.* **2013**, *23*, 245.
[36] M. R. Gao, M. K. Y. Chan, Y. Sun, *Nat. Commun.* **2015**, *6*, 7493.
[37] Y. A. Moe, Y. Sun, H. Ye, K. Liu, R. Wang, *ACS Appl. Mater. Interfaces* **2018**, *10*, 40246.
[38] A. Ali, F. A. Mangrio, X. Chen, Y. Dai, K. Chen, X. Xu, R. Xia, L. Zhu, *Nanoscale* **2019**, *11*, 7813.
[39] H. M. Oh, H. Kim, H. Kim, M. S. Jeong, *Sci. Rep.* **2019**, *9*, 5990.
[40] Y. Wang, Z. Sofer, J. Luxa, M. Pumera, *Adv. Mater. Interfaces* **2016**, *3*, 1600433.
[41] X. Chia, Z. Sofer, J. Luxa, M. Pumera, *Chem. - Eur. J.* **2017**, *23*, 11719.
[42] H. Huang, W. Huang, Z. Yang, J. Huang, J. Lin, W. Liu, Y. Liu, *J. Mater. Chem. A* **2017**, *5*, 1558.
[43] S. Radhakrishnan, P. Mane, K. A. Sree Raj, B. Chakraborty, C. S. Rout, *J. Energy Storage* **2023**, *60*, 106703.
[44] Y. Wang, F. Lu, K. Su, N. Zhang, Y. Zhang, M. Wang, X. Wang, *Chem. Eng. J.* **2020**, *399*, 126018.
[45] N. Chakrabarty, M. Char, S. Krishnamurthy, A. K. Chakraborty, *Mater. Adv.* **2021**, *2*, 366.
[46] S. Kaipannan, S. Marappan, *Sci. Rep.* **2019**, *9*, 1104.
[47] R. Sahoo, P. Acharyya, N. K. Singh, A. Pal, Y. Negishi, T. Pal, *ACS Omega* **2017**, *2*, 6576.
[48] W. Zhang, J. Xu, H. Wang, S. Yao, *J. Mater. Sci.: Mater. Electron.* **2020**, *31*, 5948.
[49] G. A. Muller, J. B. Cook, H. S. Kim, S. H. Tolbert, B. Dunn, *Nano Lett.* **2015**, *15*, 1911.
[50] V. Augustyn, J. Come, M. A. Lowe, J. W. Kim, P.-L. Taberna, S. H. Tolbert, H. D. Abruña, P. Simon, B. Dunn, *Nat. Mater.* **2013**, *12*, 518.
[51] R. Wang, S. Wang, X. Peng, Y. Zhang, D. Jin, P. K. Chu, L. Zhang, *ACS Appl. Mater. Interfaces* **2017**, *9*, 32745.
[52] M. A. Bissett, I. A. Kinloch, R. A. W. Dryfe, *ACS Appl. Mater. Interfaces* **2015**, *7*, 17388.
[53] N. Kuniyil, S. R. Koottumvathukkal Anil Raj, C. S. Rout, *Energy Fuels* **2022**, *36*, 13346.